Chemical Science

EDGE ARTICLE

View Article Online
View Journal | View Issue

Cite this: *Chem. Sci.*, 2017, **8**, 674

A low-crystalline ruthenium nano-layer supported on praseodymium oxide as an active catalyst for ammonia synthesis†

Katsutoshi Sato,*[ab] Kazuya Imamura,‡[b] Yukiko Kawano,[b] Shin-ichiro Miyahara,[a] Tomokazu Yamamoto,[c] Syo Matsumura[c] and Katsutoshi Nagaoka*[b]

Received 30th May 2016
Accepted 30th August 2016

DOI: 10.1039/c6sc02382g

www.rsc.org/chemicalscience

Ammonia is a crucial chemical feedstock for fertilizer production and is a potential energy carrier. However, the current method of synthesizing ammonia, the Haber–Bosch process, consumes a great deal of energy. To reduce energy consumption, a process and a substance that can catalyze ammonia synthesis under mild conditions (low temperature and low pressure) are strongly needed. Here we show that Ru/Pr_2O_3 without any dopant catalyzes ammonia synthesis under mild conditions at 1.8 times the rates reported with other highly active catalysts. Scanning transmission electron micrograph observations and energy dispersive X-ray analyses revealed the formation of low-crystalline nano-layers of ruthenium on the surface of Pr_2O_3. Furthermore, CO_2 temperature-programmed desorption revealed that the catalyst was strongly basic. These unique structural and electronic characteristics are considered to synergistically accelerate the rate-determining step of NH_3 synthesis, cleavage of the N≡N bond. We expect that the use of this catalyst will be a starting point for achieving efficient ammonia synthesis.

Introduction

Ammonia is one of the most important feedstocks in the modern chemical industry. Globally, >80% of ammonia produced is used to produce fertilizer, which is essential for growing crops.[1] In addition, ammonia has recently attracted attention as a carrier of energy and hydrogen.[2–5] Ammonia is produced by combining atmospheric N_2 with hydrogen produced by renewable energy. The ammonia is liquefied and transported to where it is used to generate power in engines or electricity in fuel cells. Ammonia is being considered as a carrier of energy and hydrogen because, (1) it has a high energy density (12.8 GJ m^{-3}) and (2) a high hydrogen content (17.6 wt%), and (3) carbon dioxide is not released when hydrogen is produced by ammonia decomposition.[2] If ammonia can be produced efficiently from renewable energy, it can contribute to the solution of global problems related to energy and food production.

Currently, most ammonia is synthesized *via* the Haber–Bosch process.[6–8] This process is a major consumer of energy, accounting for about 1% of global energy consumption. In this process, about 60% of consumed energy is recovered and saved in ammonia as enthalpy. However, the remaining energy is lost, mainly during the production of hydrogen from natural gas, ammonia synthesis, and gas separation. Because ammonia synthesis is carried out at very high temperatures (>450 °C) and high pressures (>20 MPa), a major goal is the reduction of the high amount of energy used in this process.[9] Curbing global energy consumption requires, *inter alia*, a catalyst that is able to produce ammonia at much lower temperatures and pressures than required for the iron-based catalysts used in the Haber–Bosch process.[10–12]

Ruthenium is a possible catalyst for ammonia synthesis because of its higher activity at low pressure and temperature compared to that of iron-based catalysts. The rate-determining step in NH_3 synthesis is cleavage of the N≡N bond of N_2, because the bond energy is very high (945 kJ mol^{-1}).[13,14] It has been reported that modification of the morphology of the Ru surface ("structural modification") and of the Ru electronic states ("electronic modification") are effective ways to accelerate the rate-determining step and thus enhance the ammonia-synthesis activity of the Ru catalyst.[15,16] In the case of structural modification, the unusual unsaturated B_5-type site of Ru has been proven to be highly active.[17–19] The B_5-type site consists of five Ru atoms: two at step edges and three on the lower terrace. The five Ru atoms are all associated with the transition state of adsorbed N_2, which results in weakening of the N≡N bond.[17]

---

[a] Elements Strategy Initiative for Catalysts and Batteries, Kyoto University, 1-30 Goryo-Ohara, Nishikyo-ku, Kyoto 615-8245, Japan

[b] Department of Applied Chemistry, Faculty of Engineering, Oita University, 700 Dannoharu, Oita 870-1192, Japan. E-mail: nagaoka@oita-u.ac.jp

[c] Department of Applied Quantum Physics and Nuclear Engineering, Kyushu University, 744 Motooka, Nishi-ku, Fukuoka 819-0395, Japan

† Electronic supplementary information (ESI) available: Detailed procedures for each method, catalytic performance, STEM-EDX images, detailed characterization. See DOI: 10.1039/c6sc02382g

‡ Present address: Research Laboratory of Hydrothermal Chemistry, Faculty of Science, Kochi University. 2-5-1 Akebono-cho, Kochi 780-8520, Japan.

Adjusting the Ru particle size (*e.g.*, to 5 nm when Ru particles are spherical) and changing the shape of Ru particles create an abundance of B_5-type sites.[18,20,21] In the case of electronic modification, the use of basic supports and the addition of a strong basic promoter to Ru catalysts have enhanced ammonia synthesis activity dramatically.[15,16] The mechanism involves the transfer of electrons to the Ru metal from the basic components. Transfer of electrons from Ru to the antibonding π-orbitals of N_2 then results in weakening of the N≡N bond and promotion of N≡N cleavage.[22] Weakening of the N≡N bond by doping with strong basic oxides has been confirmed by observation of the N≡N stretching frequency with infrared spectroscopy (IR); the most effective promoter has been reported to be Cs_2O.[23,24] In fact, most of the highly active Ru catalysts contain Cs_2O as a promoter.[10,15,25,26] However, CsOH, which may be produced in the presence of an H_2O impurity in the reactant, has a low melting point (272 °C) and may move on the surface of the catalyst particles or vaporize under the reaction conditions, the eventual result being degradation of the catalyst.[27] On the other hand, BaO is also reported as an effective promoter and Ba–Ru/activated carbon (Ba–Ru/AC) has been used in commercial industrial processes.[28] Recently, Horiuchi *et al.* reported that $Ru/BaTiO_3$ and Ba–Ru/MgO show comparable high activity to Cs–Ru/MgO.[26] Notably, Ru-loaded electride $[Ca_{24}Al_{28}O_{64}]^{4+}(e^-)_4$ (Ru/C12A7:e^-), which is a new class of Ru catalyst supported on a non-oxide, shows high NH_3-synthesis activity without any dopant.[10,29,30] This high activity has been attributed to the high electron-donating power of the electride.

We show here that a praseodymium oxide-supported Ru catalyst (Ru/Pr_2O_3) without any dopant exhibits unparalleled NH_3 synthesis ability compared with highly active catalysts reported previously. The loading of Ru on the support was characterized by an unusual morphology of low-crystalline nanolayers, and the basicity of the catalyst was very high. We show that the combination of these features facilitated the activation of N_2.

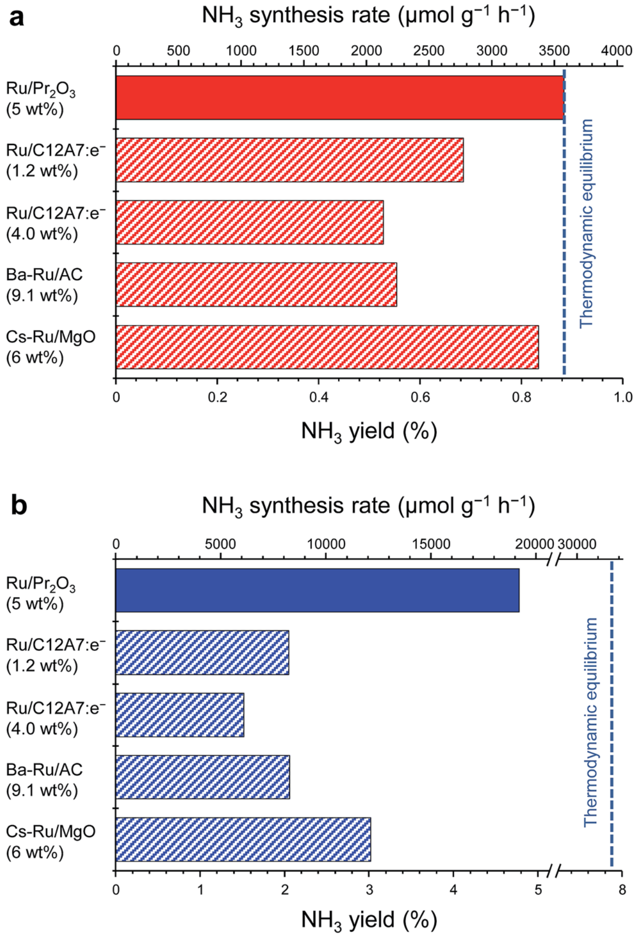

Fig. 1 Catalytic performance of supported Ru catalysts for NH_3 synthesis at (a) 0.1 MPa and (b) 1 MPa. Reaction conditions: catalyst, 0.2 g; reactant gas, $H_2/N_2 = 3$ with a flow rate of 60 mL min^{-1}; reaction temperature, 400 °C. With the exception of Ru/Pr_2O_3, NH_3 synthesis rates are reproduced from ref. 10.

Results and discussion

NH_3-synthesis activities of supported Ru-catalysts

Fig. 1 compares the NH_3-synthesis activity of the Ru/Pr_2O_3 catalyst with that of other supported Ru catalysts under the same reaction conditions. Ba–Ru/activated carbon (Ba–Ru/AC) has been used in industrial processes;[28] Cs–Ru/MgO is one of the most active Ru catalysts in NH_3 synthesis;[25,31] and Ru/C12A7:e^- has attracted attention as a new active NH_3-synthesis catalyst.[10–12] At 400 °C and 0.1 MPa (Fig. 1a), Ru/Pr_2O_3 and Cs–Ru/MgO gave NH_3 yields near the thermodynamic equilibrium (0.88%). Both the yields and NH_3 production rates were higher than those achieved with the Ru/C12A7:e^- and Ba–Ru/AC catalysts. In the industrial process, it is important to obtain high one-pass NH_3 yields to avoid the high energy usage required for gas separation. Furthermore, from the standpoint of thermodynamic regulation, NH_3 synthesis is favored if the reaction is carried out under high pressure.[9] We therefore measured the NH_3-synthesis activity at 1.0 MPa (Fig. 1b), where the NH_3 yield at the thermodynamic equilibrium increases to 7.9%. Note that 1.0 MPa is still much lower than the reaction pressure used for the Haber–Bosch process. With the increase in reaction pressure, the differences in the activities of the catalysts were more pronounced: the NH_3 yield reached 4.8% and the rate of formation obtained over Ru/Pr_2O_3 reached 19 000 μmol g^{-1} h^{-1}, >1.8 times the values associated with other catalysts.

To understand why the rates of NH_3 synthesis are so high when catalyzed by Ru/Pr_2O_3, we compared the characteristics of Ru/Pr_2O_3 with those of Ru/MgO and Ru/CeO_2. All of the catalysts were loaded with 5 wt% Ru. Among the dopant-free simple oxide-supported Ru catalysts, Ru/MgO and Ru/CeO_2 have shown relatively high NH_3-synthesis activity,[32] and CeO_2 is a rare-earth oxide like Pr_2O_3. Fig. S2† shows *in-situ* X-ray diffraction patterns of the catalysts after activation in pure H_2 at 400 °C. In the cases of Ru/MgO and Ru/CeO_2, only diffraction patterns assigned to cubic-type MgO and CeO_2 were obtained. In the case of Ru/Pr_2O_3, the diffraction peaks were attributed to rare earth C-type Pr_2O_3.[33] On the other hand, the fact that no diffraction peaks of the Ru species were apparent in the patterns of the catalyst samples suggests that the crystallite size of the loaded Ru was too small to be detected. NH_3-synthesis activities of the Ru catalysts were then measured at 0.9 MPa after reduction at 400 °C. Ru/Pr_2O_3 catalyzed NH_3 synthesis at a much higher rate than that of Ru/MgO and Ru/CeO_2 at all temperatures from 310 to 390 °C (Fig. 2). At 390 °C in particular, the NH_3 synthesis rate of Ru/Pr_2O_3 was 15 200 μmol g^{-1} h^{-1}, much higher than that of Ru/CeO_2 (7400 μmol g^{-1} h^{-1}) and Ru/MgO (1500 μmol g^{-1} h^{-1}). Furthermore, the long-term stability of the Ru/Pr_2O_3 catalyst at 390 °C under 0.9 MPa was evidenced by the fact that the rate of NH_3 synthesis was stable for 50 h (Fig. S3†).

Specific surface areas of Ru/Pr_2O_3, Ru/CeO_2, and Ru/MgO were 20.4, 33.5, and 46.4 m^2 g^{-1}, respectively (Table 1). There was no clear correlation between specific surface area and catalytic activity. Interestingly, the H/Ru ratio, a measure of Ru dispersion, was very low for Ru/Pr_2O_3 compared with that of the other catalysts. As a result, the turnover frequency of Ru/Pr_2O_3 was >3.5 times that of Ru/CeO_2 and Ru/MgO. These results suggest that the high turnover frequency of Ru/Pr_2O_3 makes the excellent rate of synthesis of NH_3 (activity per weight of catalyst) possible.

Structural properties of Ru/Pr_2O_3

As the NH_3-synthesis ability of a supported Ru catalyst is related to the morphology of the loaded Ru and the basicity of the support material, we used scanning transmission electron micrograph (STEM) observations and energy dispersive X-ray (EDX) analysis to investigate the morphology. Fig. 3 and S4† show high-angle annular dark-field (HAADF) images and EDX maps of Ru/Pr_2O_3 following treatment of the catalyst with H_2 at 400 °C. Fig. S5 and S6† show analogous images and maps of Ru/CeO_2 and Ru/MgO, respectively. A number of particles identified as Ru species by EDX were supported on MgO and CeO_2, but were seldom observed over Pr_2O_3. However, the EDX map showed that Ru was dispersed over the entire Pr_2O_3 surface. In the reconstructed overlapping EDX images, the greenish edges of the catalyst particles indicated that the surfaces of the catalyst particles were covered by the Ru species. These results suggest that the state of Ru is completely different when it is loaded over Pr_2O_3 *versus* MgO and CeO_2. To further investigate the surface morphology, we made high-resolution STEM (HR-STEM) observations (Fig. 4, and see Fig. S7–S9†). On Ru/MgO and Ru/CeO_2, the lattice fringes of the Ru species and the supports were clearly apparent. The *d* space of the Ru species was 0.21 nm, which is consistent with that of the (101) plane of metallic Ru. Mean diameters of the Ru particles were 1.8 ± 0.7 nm on Ru/MgO and 2.5 ± 0.8 nm on Ru/CeO_2. In addition, the surface of the supports of these catalysts was smooth, and changes in the lattice fringe were clearly observed on the boundaries between Ru particles and supports (Fig. 4b and c, S8 and S9†). In contrast, on Ru/Pr_2O_3, the surface of Pr_2O_3 was covered by layers of Ru rather than by particles. The fact that the lattice fringes of most parts of the Ru layers were not apparent indicated that the crystallinity of the Ru layers was low. The thickness of the Ru layers was 0.5–3 nm, and Ru particles were sometimes included in the layers. Thus, we considered that the surface of Pr_2O_3 was covered mainly with low-crystalline Ru nano-layers.

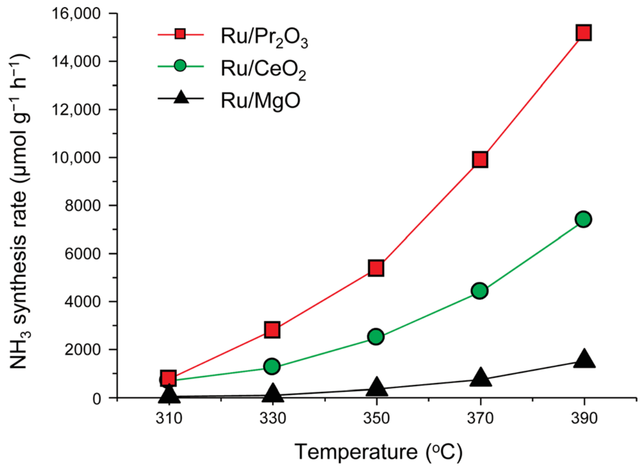

Fig. 2 Rate of NH_3 synthesis over supported Ru catalysts. Reaction conditions: catalyst, 0.2 g; reactant gas, $H_2/N_2 = 3$ with a flow rate of 60 mL min^{-1}; pressure, 0.9 MPa.

To explain why the Ru on the Pr_2O_3 support possessed such a unique morphology, we analysed the X-ray diffraction patterns of the catalyst precursors of Ru/Pr_2O_3. As shown in Fig. S10,† the bare support [before impregnation with $Ru_3(CO)_{12}$] showed the structure of fluorite-type Pr_6O_{11}. However, after impregnation with $Ru_3(CO)_{12}$ in tetrahydrofuran (THF) and drying, the peaks assigned to Pr_6O_{11} became smaller, and peaks attributed to $Pr(OH)_3$ and PrOOH appeared. Furthermore, after heat treatment under a stream of Ar at 350 °C, only peaks corresponding to PrOOH were observed. At this point, the HAADF STEM and overlay of the EDX maps of Ru/Pr_2O_3 demonstrated that the surfaces of the catalyst particles were covered by Ru species (Fig. S11†). These results indicate that $Ru_3(CO)_{12}$ reacted with the O^{2-} in Pr_6O_{11} and Pr^{4+} was reduced to Pr^{3+}, with the formation of CO_2. The support then reacted with the H_2O impurity in the THF, and after heat treatment in the Ar stream, Ru and PrOOH were formed. In brief, the results reveal that the high reactivity between $Ru_3(CO)_{12}$ and Pr_6O_{11} prevented aggregation of $Ru_3(CO)_{12}$ with $Ru_3(CO)_{12}$ and contributed to the formation of the unique structure of the loaded Ru. The rough surface of the Pr_2O_3 and the fuzziness of the boundary between Ru and Pr_2O_3 in the HR-STEM image in Fig. 4a and S7† was probably due to the reaction between $Ru_3(CO)_{12}$ and Pr_6O_{11}. Furthermore, during H_2 treatment, PrOOH was converted to Pr_2O_3 (Fig. S2†). During this process, part of the Ru included in the Ru layers was crystallized to form Ru particles, and thus Ru particles were sometimes observed in the Ru layers in the HR-STEM images (Fig. S7†). As shown in the HR-STEM images, the Ru species over Pr_2O_3 were arranged in a low-crystalline, nano-layered structure. In such a structure, unsaturated Ru atoms were not precisely arranged and formed step-and-terrace sites similar to a B_5-type site. The unique surface morphology of Ru in Ru/Pr_2O_3 would promote N_2 adsorption and subsequent cleavage of the N≡N bond.

Table 1 Physicochemical properties of supported Ru catalysts

Catalyst	Specific surface area (m^2 g^{-1})	H/Ru[a]	Turnover frequency[b] (s^{-1})	Density of base sites[c] (μmol m^{-2})
Ru/Pr_2O_3	20.4	0.17	0.050	4.4
Ru/CeO_2	33.5	0.29	0.014	2.3
Ru/MgO	46.4	0.3	0.003	2.2

[a] Estimated by using H_2 chemisorption capacity. [b] Calculated by using H/Ru value and NH_3 yield at 390 °C under 0.9 MPa. [c] Estimated by using CO_2-TPD.

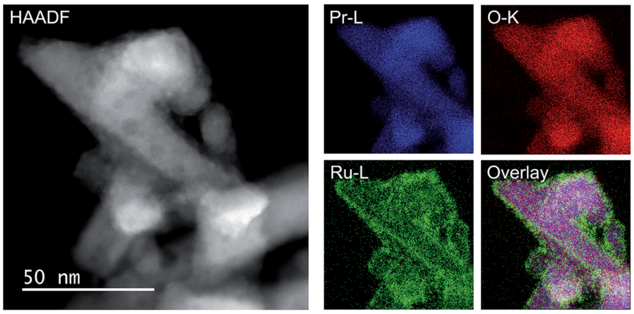

Fig. 3 HAADF-STEM image, Pr-L, O-K, and Ru-L STEM-EDX maps, and reconstructed overlay image of Pr, O, and Ru for Ru/Pr_2O_3 after H_2 reduction.

In addition, we carried out STEM-EDX observations of Ru/Pr_2O_3 after the long-term stability test shown in Fig. S3.† As shown in Fig. S12 and S13,† Pr_2O_3 was still covered with low-crystalline Ru nano-layers, as it was before reaction, and distinct changes of the structure were not observable. These results demonstrate the high durability of the unique surface structure of Ru/Pr_2O_3 under the conditions used for NH_3 synthesis.

Basic properties of Ru/Pr_2O_3

We used CO_2 temperature-programmed desorption (CO_2-TPD) measurements of the catalysts (Fig. 5) to evaluate another crucial determinant of NH_3-synthesis ability, the basicity of the support. To remove the contribution of the CO_2 that remained on the surface even after H_2 reduction, we subtracted the CO_2-TPD profile without CO_2 adsorption from that after CO_2 adsorption (see Fig. S14† for original figures). CO_2 desorption was observed at 50–680 °C on Ru/Pr_2O_3, 50–600 °C on Ru/CeO_2, and 50–500 °C on Ru/MgO. CO_2 desorption observed in the high temperature region (≥300 °C) was greatest on Ru/Pr_2O_3, intermediate on Ru/CeO_2, and least on Ru/MgO. These results indicate that the basic sites on Ru/Pr_2O_3 are the strongest, and those on Ru/MgO are the weakest. We used the total amount of CO_2 desorbed as a metric of basic density over the catalysts. Ru/Pr_2O_3 had the highest basic density, 4.4 μmol m^{-2}, almost twice that of Ru/CeO_2, 2.3 μmol m^{-2}, and Ru/MgO, 2.2 μmol m^{-2}. These results reveal that the surface basicity of Ru/Pr_2O_3 was much stronger than that of Ru/MgO and Ru/CeO_2. This strong surface basicity results in the most effective electron donation to Ru and promotes N_2 adsorption and subsequent cleavage of the N≡N bond. Furthermore, we can say that Pr_2O_3 is covered by islands of Ru nano-layers, which allow large amounts of CO_2 to adsorb on the surface of uncovered Pr_2O_3. Note also that the CO_2 desorption temperature and the total density of the basic sites were higher on Ru/CeO_2 than on Ru/MgO. This difference accounts for the higher NH_3-synthesis activity of Ru/CeO_2 than that of Ru/MgO.

Activation of N_2 over Ru/Pr_2O_3

Finally, to understand the activation of N_2 molecules over the Ru/Pr_2O_3 catalyst, we examined the states of the adsorbed N_2 with FT-IR techniques. The IR spectra after the addition of N_2 to Ru/MgO, Ru/CeO_2, and Ru/Pr_2O_3 at room temperature are shown in Fig. 6. The IR spectrum of each catalyst shows a broad peak around 2350 to 2100 cm^{-1}; such peaks are assignable to the stretching vibration mode of the N_2 adsorbed with an end-on orientation on the Ru surface.[21,23,24] Note that the peak absorbance of N_2 adsorbed on Ru/Pr_2O_3 occurred at a lower frequency (2178 cm^{-1}) than the corresponding peak absorbances on Ru/MgO (2210 cm^{-1}) and Ru/CeO_2 (2189 cm^{-1}). In the spectrum of $^{15}N_2$ adsorbed on Ru/Pr_2O_3, the peak absorbance was shifted to a lower frequency (2106 cm^{-1}) compared to

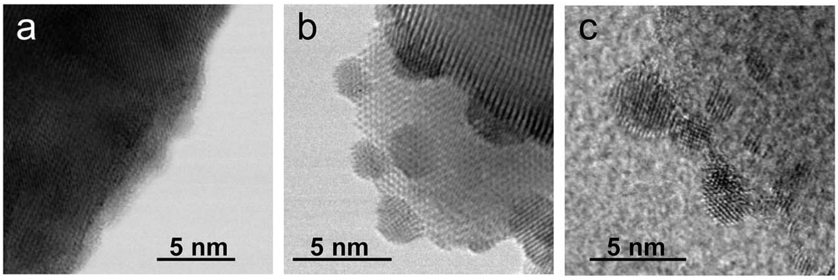

Fig. 4 HR-STEM images of (a) Ru/Pr_2O_3, (b) Ru/CeO_2, and (c) Ru/MgO, after H_2 reduction.

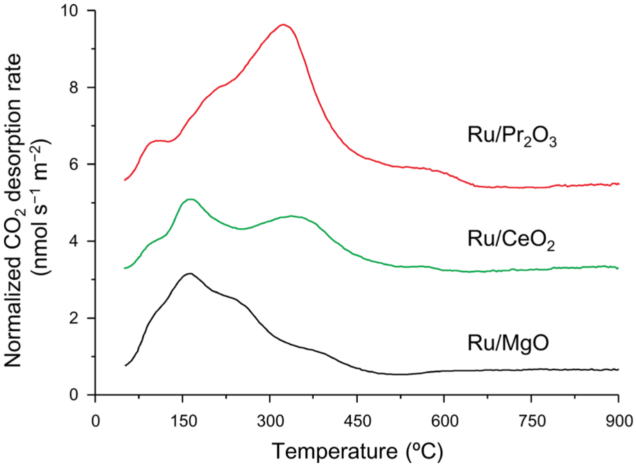

Fig. 5 CO_2-TPD profiles of supported Ru catalysts. Following H_2 reduction at 400 °C, CO_2 adsorption was carried out at 50 °C. These curves show the difference between the curves shown in Fig. S14† to remove the contribution of CO_2 that remained on the surface of the catalysts even after H_2 pre-treatment.

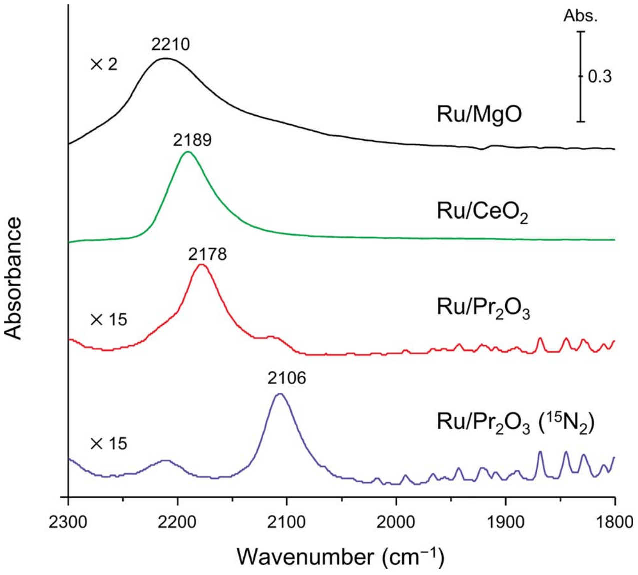

Fig. 6 Difference infrared spectra of N_2 molecules (before and after N_2 adsorption) on supported Ru catalysts. Spectra were collected under 6 kPa of N_2 ($^{15}N_2$ for Ru/Pr_2O_3) at 25 °C.

that on Ru/Pr_2O_3 (2178 cm^{-1}), which is in good agreement with the frequency estimated from the isotope effect (2178 cm^{-1} × $(14/15)^{1/2}$ = 2104 cm^{-1}).[23,24] These results suggest that these peaks are associated with the N_2 on the Ru surfaces. The lower frequencies of the peak absorbances of N_2 adsorbed on Ru/Pr_2O_3 compared to those of Ru/MgO and Ru/CeO_2 indicate that the N≡N bond of N_2 was further weakened over the low-crystalline Ru nano-layers on Pr_2O_3 relative to Ru nanoparticles on the other supports. We surmise that the morphology of the Ru surface and the basicity of the catalyst contributed synergistically to the weakening of the N≡N bond and enhanced the catalytic activity for NH_3 synthesis.

Conclusions

In summary, we demonstrated that Ru/Pr_2O_3 without any dopant catalyzed a high rate of NH_3 synthesis under mild reaction conditions (0.1–1.0 MPa). Characteristics of Ru/Pr_2O_3 include low-crystalline Ru nano-layers formed by the reaction between $Ru_3(CO)_{12}$ and Pr_6O_{11} and strong basicity of Pr_2O_3. These characteristics are considered to synergistically accelerate the rate-determining step of ammonia synthesis: cleavage of the N≡N bond of N_2. In addition, substitution of some of the praseodymium with another element without degrading its activity for NH_3 synthesis is currently in progress, because Pr is an expensive element. The outcome of the research will appear in a coming contribution. We believe that our catalyst will facilitate the development of an effective method for synthesizing ammonia from renewable energy under environmentally benign conditions. Such a method can be expected to contribute to the solution of food and energy crises globally.

Acknowledgements

This work was supported by CREST, Japan Agency of Science and Technology (JST). STEM/TEM observations were performed as part of a program conducted by the Advanced Characterization Nanotechnology Platform Japan, sponsored by the Ministry of Education, Culture, Sports, Science and Technology (MEXT), Japan. K. Sato thanks the Program for the Elements Strategy Initiative for Catalysts & Batteries (ESICB) commissioned by MEXT. T. Toriyama (Kyushu University) is acknowledged for assistance with STEM/TEM observations. The authors thank Mr Y. Wada, Ms. M. K. Nakao, and Mr T. Terasawa (Oita University) for assistance with sample preparation, catalytic activity tests, and characterization techniques. We acknowledge Prof. K. Shimizu (Hokkaido University) for fruitful discussions concerning IR analysis.

Notes and references

1 J. W. Erisman, M. A. Sutton, J. Galloway, Z. Klimont and W. Winiwarter, *Nat. Geosci.*, 2008, **1**, 636–639.
2 A. Klerke, C. H. Christensen, J. K. Nørskov and T. Vegge, *J. Mater. Chem.*, 2008, **18**, 2304–2310.
3 R. Schlogl, *ChemSusChem*, 2010, **3**, 209–222.
4 F. Schüth, R. Palkovits, R. Schlögl and D. S. Su, *Energy Environ. Sci.*, 2012, **5**, 6278–6289.
5 J. W. Makepeace, T. J. Wood, H. M. A. Hunter, M. O. Jones and W. I. F. David, *Chem. Sci.*, 2015, **6**, 3805–3815.
6 H. Bielawa, O. Hinrichsen, A. Birkner and M. Muhler, *Angew. Chem., Int. Ed.*, 2001, **40**, 1061–1063.
7 T. Kandemir, M. E. Schuster, A. Senyshyn, M. Behrens and R. Schlogl, *Angew. Chem., Int. Ed.*, 2013, **52**, 12723–12726.
8 S. Perathoner and G. Centi, *ChemSusChem*, 2014, **7**, 1274–1282.
9 C. W. Hooper, Ammonia Synthesis: Commercial Practice, in *Catalytic Ammonia Synthesis, Fundamentals and Practice*, ed. J. R. Jennings, Springer, US, 1991, pp. 253–283.

10 M. Kitano, Y. Inoue, Y. Yamazaki, F. Hayashi, S. Kanbara, S. Matsuishi, T. Yokoyama, S. W. Kim, M. Hara and H. Hosono, *Nat. Chem.*, 2012, **4**, 934–940.

11 F. Hayashi, M. Kitano, T. Yokoyama, M. Hara and H. Hosono, *ChemCatChem*, 2014, **6**, 1317–1323.

12 Y. Inoue, M. Kitano, S.-W. Kim, T. Yokoyama, M. Hara and H. Hosono, *ACS Catal.*, 2014, **4**, 674–680.

13 S. Gambarotta and J. Scott, *Angew. Chem., Int. Ed.*, 2004, **43**, 5298–5308.

14 H. K. Chae, D. Y. Siberio-Perez, J. Kim, Y. Go, M. Eddaoudi, A. J. Matzger, M. O'Keeffe and O. M. Yaghi, *Nature*, 2004, **427**, 523–527.

15 K. Aika, H. Hori and A. Ozaki, *J. Catal.*, 1972, **27**, 424–431.

16 K. Aika, M. Kumasaka, T. Oma, O. Kato, H. Matsuda, N. Watanabe, K. Yamazaki, A. Ozaki and T. Onishi, *Appl. Catal.*, 1986, **28**, 57–68.

17 S. Dahl, A. Logadottir, R. C. Egeberg, J. H. Larsen, I. Chorkendorff, E. Törnqvist and J. K. Nørskov, *Phys. Rev. Lett.*, 1999, **83**, 1814–1817.

18 C. J. H. Jacobsen, S. Dahl, P. L. Hansen, E. Törnqvist, L. Jensen, H. Topsøe, D. V. Prip, P. B. Møenshaug and I. Chorkendorff, *J. Mol. Catal. A: Chem.*, 2000, **163**, 19–26.

19 S. Dahl, E. Tornqvist and I. Chorkendorff, *J. Catal.*, 2000, **192**, 381–390.

20 Z. Song, T. Cai, J. C. Hanson, J. A. Rodriguez and J. Hrbek, *J. Am. Chem. Soc.*, 2004, **126**, 8576–8584.

21 Z. You, K. Inazu, K. Aika and T. Baba, *J. Catal.*, 2007, **251**, 321–331.

22 K. Aika, A. Ohya, A. Ozaki, Y. Inoue and I. Yasumori, *J. Catal.*, 1985, **92**, 305–311.

23 J. Kubota and K. Aika, *J. Chem. Soc., Chem. Commun.*, 1991, 1544.

24 J. Kubota and K. Aika, *J. Phys. Chem.*, 1994, **98**, 11293–11300.

25 K. Aika, T. Takano and S. Murata, *J. Catal.*, 1992, **136**, 126–140.

26 Y. Horiuchi, G. Kamei, M. Saito and M. Matsuoka, *Chem. Lett.*, 2013, **42**, 1282–1284.

27 J. G. van Ommen, W. J. Bolink, J. Prasad and P. Mars, *J. Catal.*, 1975, **38**, 120–127.

28 D. E. Brown, T. Edmonds, R. W. Joyner, J. J. McCarroll and S. R. Tennison, *Catal. Lett.*, 2014, **144**, 545–552.

29 M. Kitano, Y. Inoue, H. Ishikawa, K. Yamagata, T. Nakao, T. Tada, S. Matsuishi, T. Yokoyama, M. Hara and H. Hosono, *Chem. Sci.*, 2016, **7**, 4036–4043.

30 Y. Lu, J. Li, T. Tada, Y. Toda, S. Ueda, T. Yokoyama, M. Kitano and H. Hosono, *J. Am. Chem. Soc.*, 2016, **138**, 3970–3973.

31 F. Rosowski, A. Hornung, O. Hinrichsen, D. Herein, M. Muhler and G. Ertl, *Appl. Catal., A*, 1997, **151**, 443–460.

32 Y. Niwa and K.-i. Aika, *Chem. Lett.*, 1996, **25**, 3–4.

33 G. Adachi and N. Imanaka, *Chem. Rev.*, 1998, **98**, 1479–1514.